Results in Physics 8 (2018) 253–256

Contents lists available at ScienceDirect

Results in Physics

journal homepage: www.journals.elsevier.com/results-in-physics

# Excellent glass forming ability and plasticity in high entropy $Zr_{20}Ti_{20}Hf_{20}M_{20}Be_{20}$ (M = Cu, Ni, Co) alloys

Haitao Zong [a], Chenchen Geng [a], Chaoyang Kang [a], Guohua Cao [a], Linyan Bian [b,*], Lixin Li [c], Baoqing Zhang [c], Ming Li [a,*]

[a] School of Physics and Electronic Information, Henan Polytechnic University, Jiaozuo 454000, China
[b] School of Chemistry and Chemical Engineering, Henan Polytechnic University, Jiaozuo 454000, China
[c] School of Materials Science and Engineering, Henan Polytechnic University, Jiaozuo 454000, China

ARTICLE INFO

*Article history:*
Received 8 November 2017
Received in revised form 1 December 2017
Accepted 2 December 2017
Available online 6 December 2017

*Keywords:*
High entropy alloys
Bulk metallic glasses
Glass forming ability
Mechanical property and fragility

ABSTRACT

We reported here the studies of a series of $Zr_{20}Ti_{20}Hf_{20}M_{20}Be_{20}$ (M = Cu, Ni and Co) quinary high entropy bulk metallic glasses. Glasses with critical diameters ($D_c$) of 3 mm, 8 mm and 5 mm, respectively has been successfully fabricated by copper mold casting. Strikingly, a plastic strain of 11.6% is achieved in the $Zr_{20}Ti_{20}Hf_{20}Cu_{20}Be_{20}$ metallic glass. The dynamic fragility the $Zr_{20}Ti_{20}Hf_{20}Cu_{20}Be_{20}$ alloy is determined from calorimetric measurements. The excellent plasticity is explained to be attributed to relatively higher fragility.



## Introduction

High entropy alloys (HEAs) are metallic solid solutions composed by five or more elements of equal (or nearly equal) atomic mole fraction, and usually possess simple face-centered cubic or body-centered cubic lattice structures. Such alloys have triggered a lot of expectations as potential new family of structural component materials due to unique physical and mechanical properties which result from their multi-component nature [1–4]. A series of excellent properties such as high hardness and strength [1,5–7], good resistance to softening at high temperature [5,8–10], outstanding wear and fatigue properties [11], good corrosion resistance [12] and biocompatibility [13] have been exhibited. It appears that the concept of "high entropy" introduces a new way to develop advanced metallic materials with unique physical and mechanical properties.

Recently, the experimental studies show that the high entropy alloys could be used to develop novel bulk metallic glasses (BMGs) with certain glass forming ability (GFA) [14–20]. However, most of the reported "high entropy bulk metallic glasses (HE-BMGs)" have a critical size $D_c$ of less than 5 mm and a compressive plasticity strain of less than 3% [15,19,21]. It appears that the optimal combination of high entropy alloys and glass formation still remain unclear, notwithstanding, the application potential. In the present study, we studied a new series of $Zr_{20}Ti_{20}Hf_{20}M_{20}Be_{20}$ (M = Cu, Ni and Co) quinary high entropy alloys, aiming at developing the understanding of the glass formation in the high entropy alloys, and found that the addition of Cu, Ni and C0 can enhance effectively glass forming ability, in particular, excellent mechanical properties is observed in the $Zr_{20}Ti_{20}Hf_{20}Cu_{20}Be_{20}$alloys.

## Experimental procedure

Ingots of a series of alloys with nominal composition of $Zr_{20}Ti_{20}Hf_{20}M_{20}Be_{20}$ (M = Cu, Ni and Co) were prepared by arc-melting the mixtures consisting of pure elements with purities above 99.9% in a Ti gettered high-purity argon atmosphere. To achieve chemical homogeneity, all ingots were re-melted at least four times, and then suction-cast into copper molds to form rod-shaped samples with different diameters. Glassy structure and crystallization phases were examined by X-ray diffraction (XRD) using Cu K$\alpha$ radiation. Glass transition, crystallization and melting behavior of as-cast samples were characterized by differential scanning calorimetry (DSC, Netzsch STA 449C) under flowing purified argon with a heating rate of 20 K/min. The values of glass transition temperatures $T_g$, onset temperatures of the crystallization $T_x$ and liquidus temperature $T_l$ were derived from the DSC curve. The compression tests were conducted by using Instron 5582 testing

* Corresponding authors.
*E-mail addresses:* bianlinyan@hpu.edu.cn (L. Bian), mingli4587@aliyun.com (M. Li).

https://doi.org/10.1016/j.rinp.2017.12.002
2211-3797/

machine at a strain rate of $1 \times 10^{-4}\ s^{-1}$. At least three samples were tested for each composition to get a statistical result. The compression specimens with diameter of 3 mm and a length of 6 mm were cut from the as-cast rods, and the ends were polished carefully to ensure parallelism. The deformed specimens were observed with scanning electron microscope (SEM). The heating heat capacity curves are recorded around the glass transitions using a Perkin-Elmer (PE) Diamond Differential Scanning Calorimeter (DSC) calibrated by indium and cyclohexane. In order to avoid the crystallization in the $Zr_{20}Ti_{20}Hf_{20}Cu_{20}Be_{20}$ metallic glasses during heating, a relatively narrow temperature scanning range is set with the upper limit 10 K lower than the $T_x$.

## Results and discussion

Fig. 1 shows the XRD spectra of the as-cast $Zr_{20}Ti_{20}Hf_{20}M_{20}Be_{20}$ (M = Cu, Ni and Co) rods with different diameters. It can be seen that the ϕ5 mm rod of $Zr_{20}Ti_{20}Hf_{20}Cu_{20}Be_{20}$ HEA and the ϕ8 mm rod of $Zr_{20}Ti_{20}Hf_{20}Ni_{20}Be_{20}$ HEA are of full amorphous structure. The critical size (5 mm) of the $Zr_{20}Ti_{20}Hf_{20}Cu_{20}Be_{20}$ HEA is less than 12 mm which was reported by Zhao et al. in their recent studies [20]. Sharp diffraction peaks corresponding to crystalline phases were observed on the XRD spectrum of the ϕ5 mm rod of $Zr_{20}Ti_{20}Hf_{20}Co_{20}Be_{20}$ HEA, while no sharp diffraction peak (shown in the inset) but a typical broad halo pattern could be observed on the ϕ3 mm rod.

Thermal analysis of the $Zr_{20}Ti_{20}Hf_{20}M_{20}Be_{20}$ (M = Cu, Ni and Co) HE-BMGs was carried out and the obtained DSC curves were shown in Fig. 2. The relevant thermal parameters such as the glass transition temperature, $T_g$, the crystallization onset temperature, $T_x$ and the liquidus temperature, $T_l$ can be determined. Several exothermic peaks after the glass transition indicate the crystallization in the supercooled liquid regions. The thermal parameters measured from the DSC curves are summarized in Table 1 together with the critical diameter, $D_c$, supercooled liquid region, $\Delta T_x$, the GFA parameter, $\gamma$, the reduced glass transition temperature, $T_{rg}$ and plastic strain, $\varepsilon_p$. It was found that the GFA did not correlate with the $\Delta T_x$ and $T_{rg}$, but was roughly relevant to the $\gamma$ parameter, which was consistent with the investigations by Lu et al. [22].

The compressive stress-strain curves for the three HE-BMGs at room temperature are shown in Fig. 3. Similar elastic deformation can be seen for the three HE-BMGs when the strain is small, however, the remarkable difference is shown for the plastic deformation prior to failure. It can be seen clearly that while the $Zr_{20}Ti_{20}Hf_{20}Cu_{20}Be_{20}$ HE-BMG shows a large plastic strain as high as 11.6% with the fracture strength of 1885 MPa. The fracture strength and plastic strain of the $Zr_{20}Ti_{20}Hf_{20}Ni_{20}Be_{20}$ HE-BMG are 2140 MPa and 2.3%, respectively. However, the $Zr_{20}Ti_{20}Hf_{20}Co_{20}Be_{20}$ HE-BMG shows a typical brittle fracture behavior with a relative lower fracture strength and nearly no plastic strain. Fig. 4(a)–(c) shows the SEM images of the side views of Cu20, Ni20 and Co20 HE-BMGs with a diameter of 3 mm after compression tests. As shown in Fig. 4(a), for the Cu20 HE-BMG a number of shear bands roughly parallel to the major shear band are observed near the fracture surface. For the Ni20 HE-BMG, only a few shear bands (Fig. 4(b)) appear on the side surface. And for the Co20 HE-BMG with practically no plastic strain, there is no shear bands can be seen on the outer surface (Fig. 4(c)). The fracture surface of the Cu20 and Ni20 HE-BMGs are shown in Fig. 4(d) and (e), a vein-like pattern with a rather uniform arrangement can be observed, indicating a typical shear fracture mechanism. As for Co20 HE-BMG, different fracture surface profiles (Fig. 4(f)), i.e. a dimple-like structure, a periodic corrugation pattern and a pure mirror zone can be observed, implying the brittle nature of Co20 HE-BMG [23].

To explain the excellent plasticity of the $Zr_{20}Ti_{20}Hf_{20}Cu_{20}Be_{20}$ HE-BMG, the kinetic factors and the fragility *m* are studied by DSC measurements. Fig. 5(a) shows the heating heat capacity curves of the $Zr_{20}Hf_{20}Ti_{20}Cu_{20}Be_{20}$ quenched at different cooling rates with a fixed heating rate of 20 K/min. In the method described in Ref. [24], a standard scan and a standard fictive temperature $T_f$ are defined using the Moynihan method [25] and then the fictive temperatures for runs of different cooling rates $q_c$ are assessed by an enthalpy differencing procedure. The differences $\Delta H(q)$ (which is the enthalpy release from the nonstandard sample if the cooling rate $-q$ exceeded that of the standard scan) are obtained from the differences between the heating heat capacity of glasses quenched at other cooling rates and of the reference glass [24], the heating heat differences are shown Fig. 5(b). Note that the $\Delta C_p$ of Ni20 and Co20 HE-BMGs are difficult to determine from the heat flow because Ni20 and Co20 HE-BMGs crystallize immediately above the $T_g$, leaving no overshoot and no stable supercooled liquid region on the up scan. Fig. 5(c) shows the activation energy plot built by the reciprocal fictive temperature $T_f$ and

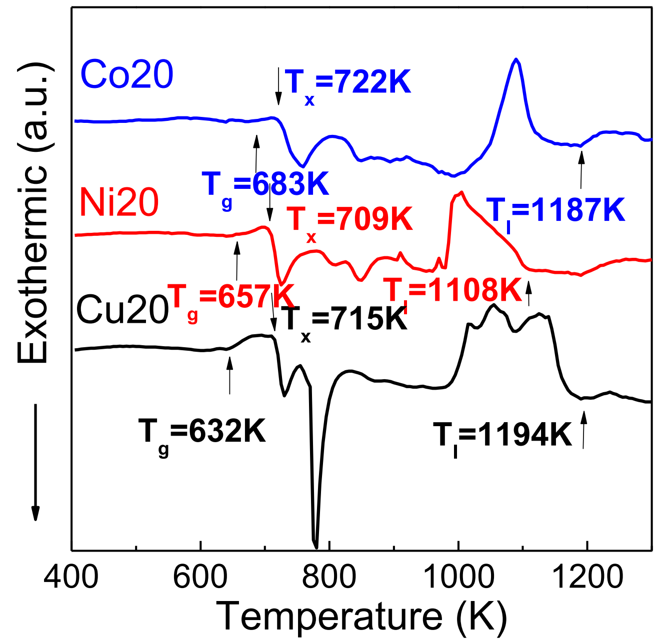


**Fig. 2.** DSC traces for the $Zr_{20}Ti_{20}Hf_{20}M_{20}Be_{20}$ (M = Cu, Ni and Co) metallic glasses, with diameters of 3 mm, obtained at a heating rate of 20 K/min.

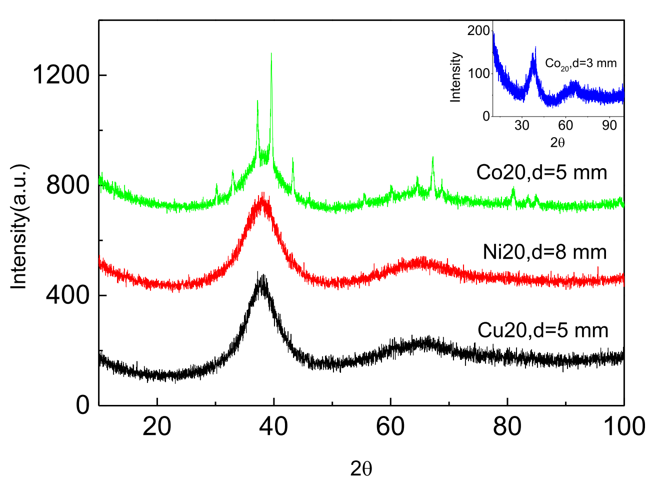


**Fig. 1.** XRD patterns for the $Zr_{20}Ti_{20}Hf_{20}M_{20}Be_{20}$ (M = Cu, Ni and Co) alloys, taken from rods with diameters of 3 mm, 5 mm and 8 mm.

**Table 1**
Thermal properties, mechanical properties and the critical diameters of the $Zr_{20}Ti_{20}Hf_{20}M_{20}Be_{20}$ (M = Cu, Ni and Co) HE-BMGs.

| Compositions | $D_c$ (mm) | $T_g$ (K) | $T_x$ (K) | $T_l$ (K) | $\Delta T_x$ | $T_{rg}$ | $\gamma$ | $\varepsilon_p$ (%) |
|---|---|---|---|---|---|---|---|---|
| $Zr_{20}Ti_{20}Hf_{20}Cu_{20}Be_{20}$ | 5 | 632 | 715 | 1194 | 83 | 0.53 | 0.39 | 11.6 |
| $Zr_{20}Ti_{20}Hf_{20}Ni_{20}Be_{20}$ | 8 | 657 | 709 | 1108 | 52 | 0.59 | 0.44 | 2.3 |
| $Zr_{20}Ti_{20}Hf_{20}Co_{20}Be_{20}$ | 3 | 683 | 722 | 1187 | 39 | 0.57 | 0.37 | 0 |

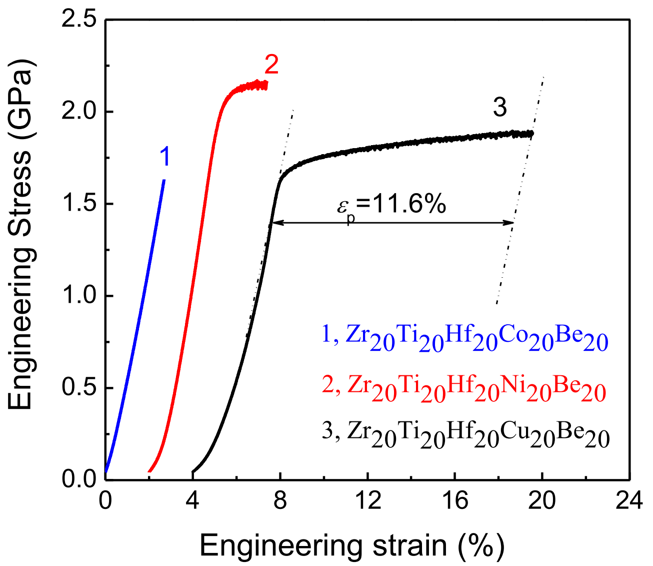


**Fig. 3.** Compressive stress-strain curves for the as-cast $Zr_{20}Ti_{20}Hf_{20}M_{20}Be_{20}$ (M = Cu, Ni and Co) glassy rods (3 mm in diameter and 6 mm in length) obtained at a strain rate of $1 \times 10^{-4}$ $s^{-1}$ at room temperature.

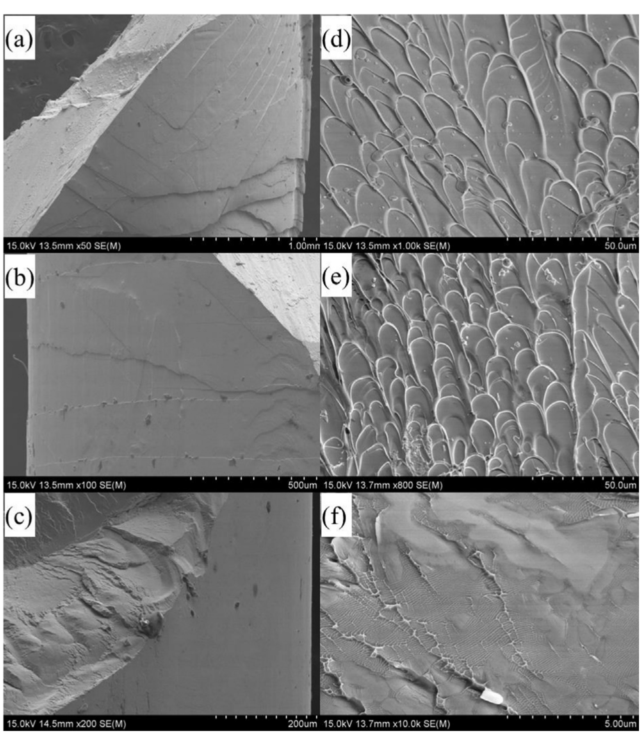


**Fig. 4.** SEM observations revealing the compressive fracture feature of $Zr_{20}Ti_{20}Hf_{20}M_{20}Be_{20}$ (M = Cu, Ni and Co) HE-BMGs, respectively. (a)–(c)shear bands on the outer surface; (d)–(f) compressive fracture surface.

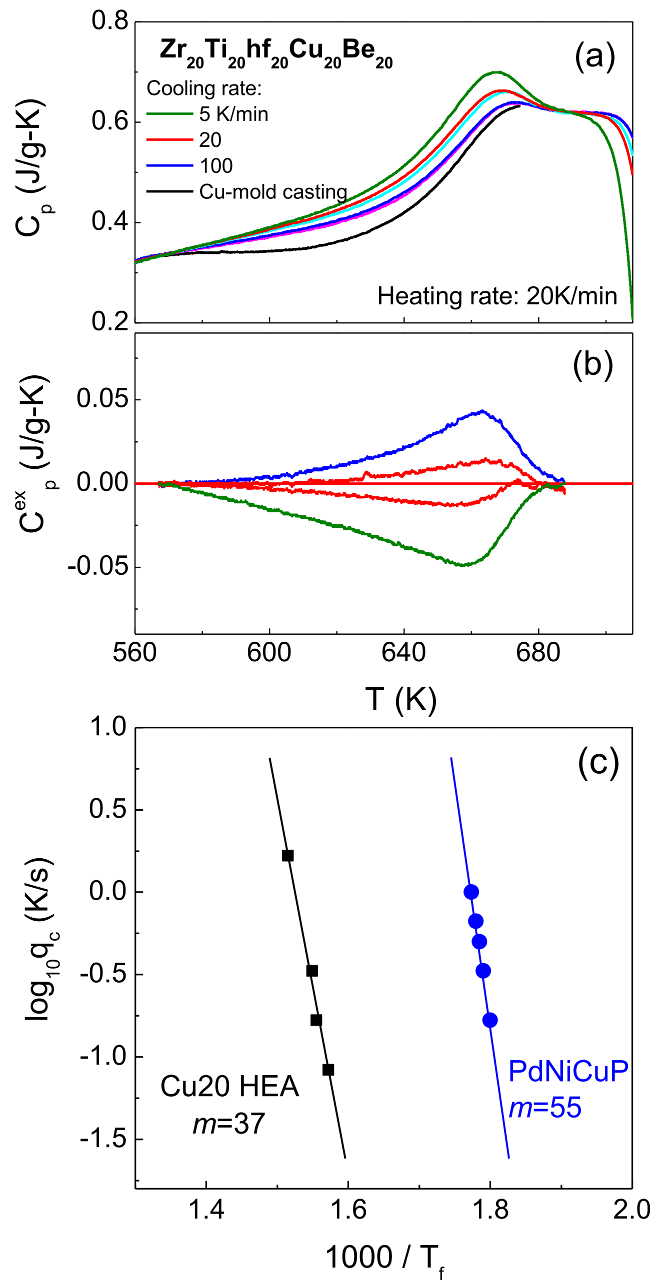


**Fig. 5.** (a) Heating heat capacity $C_p$ curves of $Zr_{20}Ti_{20}Hf_{20}Cu_{20}Be_{20}$ quenched at different cooling rates. (b) $C_p$ difference between the glass quenched from a cooling of 20 K/min and the glasses quenched at other rates. (c) The fictive temperature dependence of cooling rate.

the cooling rates $q_c$ for $Zr_{20}Hf_{20}Ti_{20}Cu_{20}Be_{20}$ HE-BMG, and the fragility $m$ = 37 is obtained from the slopes [24], showing a strong liquid. For comparison, the data of $Pd_{39}Ni_{10}Cu_{30}P_{21}$ [25] is also shown.

By using the fragility parameter ($m$), the supercooled liquid can be classified as strong or fragile. Metallic glasses typically have $m$ values in the range of 32–66 and were classified in the intermediate category according to Angell's classification scheme [26].The $m$ value of Cu20 HE- BMG is following this classification. Some papers have reported the relationship between fragility and plasticity of

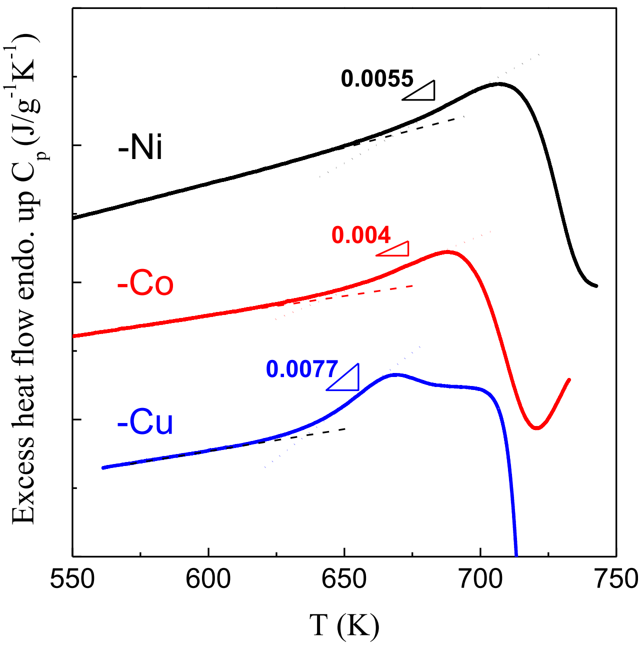


**Fig. 6.** Excess heat flow measured by DSC upon heating at 20 K/min after a proceeding cooling at 20 K/min ($q_h = q_c$) for $Zr_{20}Ti_{20}Hf_{20}M_{20}Be_{20}$ (M = Cu, Ni and Co) HE-BMGs.

BMGs [27]. It was found that the ductile BMGs could be viewed as a mixture of "solid like" and "liquid like" structural entities. Generally, BMGs with higher *m* value have a larger Possion's ratio and allows shear collapse before the extensional instability of crack formation occurs [28,29]. Namely, fragile metallic glasses with higher *m* value need less debonding energy inside a shear band due to their relatively weak atomic bonding, which furthermore favors the formation of a large amount of shear transition zones [30]. This would cause the formation of multiple shear bands, which results in large plasticity.

In our experiment, the *m* indexs of the $Zr_{20}Ti_{20}Hf_{20}M_{20}Be_{20}$ (M = Cu, Ni and Co) HE-BMGs are determined calorimetrically via the $T_f$ method rather than $T_{g\text{-}onset}$ method. As mentioned above, the *m* indexs for the Ni20 and Co20 HE-BMGs are hard to determine due to that there are no overshoot and no stable supercooled liquid region on the up scan. Recently, Shuai et al. found that the liquid fragility was well correlated with the scaled maximum slope of the DSC heat flow during the glass transition [31]. In Fig. 6., the excess heat flow was plotted against the absolute temperatures ranging from 550 K to 750 K and also the calculated maximum slopes for Cu20, Ni20 and Co20 HE BMGs were 0.0077, 0.0055 and 0.004, respectively. It can be derived that the *m* values of the three HE-BMGs are in turn as follows: $m_{Cu20} > m_{Ni20} > m_{Co20}$. Therefore, the excellent plasticity of Cu20 HE-BMG in our study can be attributed to its relatively higher fragility.

## Conclusions

A series of $Zr_{20}Ti_{20}Hf_{20}M_{20}Be_{20}$ (M = Cu, Ni and Co) quinary HE-BMGs were successfully prepared by copper mold casting. The $Zr_{20}Ti_{20}Hf_{20}Ni_{20}Be_{20}$ alloy exhibits the largest critical diameter of 8 mm. The $Zr_{20}Ti_{20}Hf_{20}Cu_{20}Be_{20}$ HE-BMG has the largest plastic elongation of 11.3% and the excellent plasticity is attributed to its relatively higher fragility index.

## Acknowledgments

This work was supported by the National Natural Science Foundation of China (11405045, 51571085, 51301062 and 11304081), the Program for Innovative Research Team of Henan Polytechnic University (No. T2017-2), the Fundamental Research Funds for the Universities of Henan Province (NSFRF1618) and the Doctoral fund project of (No. B2013-046).

## References

[1] Yeh JW, Chen SK, Lin SJ, Gan JY, Chin TS, Shun TT, et al. Adv Eng Mater 2004;6:299.
[2] Cantor B, Chang ITH, Knight P, Vincent AJB. Mater Sci Eng 2004;375–377:213.
[3] Zhao YJ, Qiao JW, Ma SG, Gao MC, Yang HJ, Chen MW, et al. Mater Des 2016;96:10.
[4] Qiao JW, Jia HL, Liaw PK. Mater Sci Eng R 2016;100:1.
[5] Tsai MH, Yeh JW. Mater Res Lett 2014;2:107.
[6] Tang Z, Gao MC, Diao H, Yang T, Liu J, Zou T, et al. JOM 2013;65:1848.
[7] Zhang Y, Zuo TT, Tang Z, Gao MC, Dahmen KA, Liaw PK, et al. Prog Mater Sci 2014;61:1.
[8] Senkov ON, Wilks GB, Scott JM, Miracle DB. Intermetallics 2011;19:698.
[9] Senkov ON, Scott JM, Senkova SV, Miracle DB, Woodward CF. J Alloy Compd 2011;509:6043.
[10] Senkov ON, Senkova SV, Miracle DB, Woodward CF. Mater Sci Eng 2013;565:51.
[11] Hemphill MA, Yuan T, Wang GY, Yeh JW, Tsai CW, Chuang A, et al. Acta Mater 2012;60:5723.
[12] Lee CP, Chang CC, Chen YY, Yeh JW, Shih HC. Corros Sci 2008;50:2053.
[13] Braic V, Balaceanu M, Braic M, Vladescu A, Panseri S, Russo A. J Mech Behav Biomed Mater 2012;10:197.
[14] Qiao JC, Pelletier JM, Li N, Yao Y. J Iron Steel Res Int 2016;23:19.
[15] Gao XQ, Zhao K, Ke HB, Ding DW, Wang WH, Bai HY. J Non-Cryst Solids 2011;357:3557.
[16] Li HF, Xie XH, Zhao K, Wang YB, Zheng YF, Wang WH, et al. Acta Biomater 2013;9:8561.
[17] Cao JW, Han JG, Guo ZH, Zhao WB, Guo YQ, Xia ZH, et al. Mater Sci Eng A 2016;673:141.
[18] Wang J, Zheng Z, Xu J, Wang Y. J Magn Magn Mater 2014;355:58.
[19] Ding HY, Yao KF. J Non-Cryst Solids 2013;364:9.
[20] Zhao SF, Gang GN, Ding HY, Yao KF. Intermetallics 2015;61:47.
[21] Ma LQ, Wang LM, Zhang T, Inoue A. Mater Trans 2002;43:277.
[22] Lu ZP, Liu CT. Acta Mater 2002;50:3501.
[23] Wang G, Chan KC, Xu XH, Wang WH. Acta Materialia 2008;56:5845.
[24] Wang LM, Velikov V, Angell CA. J Chem Phys 2002;117:10184.
[25] Chen ZM, Li ZJ, Zhang Y, Liu RP, Tian YJ, Wang LM. Eur Phys J E 2014;37:52.
[26] Angell CA. J Non-Cryst Solids 1985;73:1.
[27] Na JH, Park ES, Kim YC, Fleury E, Kim WT, Kim DH. J Mater Res 2008;23:523.
[28] Park ES, Lee JY, Kim DH, Gebert A, Schultz L. J Appl Phys 2008;104:023520.
[29] Schroers J, Johnson WL. Phys Rev Lett 2004;93:255506.
[30] Zhu SL, Xie GQ, Qin FX, Wang XM, Inoue A. J Mech Behav Biomed Mater 2012;13:166.
[31] Shuai W, Everson Z, Gallino I, Busch R. Intermetallics 2014;55:138.